

TiO₂-Fe₂O₃ nanocomposites as high-capacity negative electrode materials for rechargeable sodium-ion batteries

 C.S. Ding,^a T. Nohira^{b,*} and R. Hagiwara^{a,*}

 Received 00th January 20xx,
Accepted 00th January 20xx

DOI: 10.1039/x0xx00000x

www.rsc.org/

In this study, we report TiO₂-Fe₂O₃ nanocomposites as high-capacity negative electrode materials for rechargeable sodium-ion batteries with ionic liquid electrolyte. The TiO₂-Fe₂O₃ electrode in Na[FSA]-[C₃C₁pyrr][FSA] (FSA = bis(fluorosulfonyl)amide; C₃C₁pyrr = *N*-methyl-*N*-propylpyrrolidinium) ionic liquid electrolyte at 363 K delivers a high reversible capacity exceeding 360 mAh g⁻¹ at a current density of 10 mA g⁻¹, exhibiting good rate capability and cycling performance.

Introduction

The development and utilization of renewable energy, such as solar energy and wind energy, will play a key role in meeting future energy demand and protecting environment. Energy storage, especially battery storage, is one of the key technologies in developing renewable energy. Rechargeable sodium-ion batteries (SIBs), as a replacement for lithium-ion batteries, are attracting much attention as large-scale power storage devices for applications in electric vehicles and stationary energy storage, because sodium is a more abundant natural resource than lithium. The major challenge for the practical application of SIBs is the development of new active materials with large capacities, long cycle lives, and excellent rate capabilities. Although numerous materials have been reported as negative electrodes for SIBs, none of them display sufficiently high capacity, good cycling performance, adequate charge-discharge potential, good rate capability, natural abundance, etc. Alloy materials^{1–4} exhibit high reversible capacities; however, they also suffer from low cycling performance due to the large volume changes that occur during charge-discharge cycles. Carbon materials,^{5–9} e.g., hard carbon,^{8,9} were also investigated as negative electrode materials, showing reversible capacities of 200–300 mAh g⁻¹. Nevertheless, carbon materials always exhibit low volumetric performance because of their relatively low density. Moreover, hard carbon negative electrodes also tend to show a potential plateau below 0.1 V vs. Na/Na⁺, raising safety issues because of metallic sodium plating and dendrite formation. Some sodium titanium oxides such as Na₂Ti₃O₇^{10–12} and NaTiO₂¹³ were also investigated as alternative negative electrode materials, showing reversible capacities below 200 mAh g⁻¹ and poor rate

capabilities.

Iron oxide, Fe₂O₃, is considered a promising negative electrode candidate for SIBs because of its abundance, low cost, high theoretical capacity (1007 mAh g⁻¹), and non-toxicity. Valvo *et al.*¹⁴ reported a nanostructured Fe₂O₃ negative electrode with a reversible capacity of about 420 mAh g⁻¹ at 40 mA g⁻¹. Jian *et al.*¹⁵ reported Fe₂O₃ nanocrystals anchored onto graphene nanosheets as a negative electrode material for SIBs, with a reversible capacity of 535 mAh g⁻¹ at 100 mA g⁻¹. Jiang *et al.*¹⁶ investigated a porous Fe₂O₃ thin film negative electrode, obtaining a reversible capacity of 550 mAh g⁻¹ at 50 mA g⁻¹. Despite exhibiting high reversible capacities, Fe₂O₃ electrodes usually suffer from a large volume change during Na-ion insertion/extraction, which leads to the rapid agglomeration of metal oxide particles and pulverization of electrode materials, finally causing capacity loss and deteriorated cycling performance.^{15,17}

Recently, titanium dioxides, including amorphous TiO₂,¹⁸ TiO₂ (B),¹⁹ TiO₂ (H),²⁰ anatase TiO₂,^{21–24} and Nb-doped rutile TiO₂,²⁵ were investigated as negative electrode materials for SIBs, with anatase TiO₂ showing the highest reversible capacity. Xu *et al.*²¹ investigated nanocrystalline anatase TiO₂ and reported a reversible discharge capacity of about 150 mAh g⁻¹. Kim *et al.*²² reported that an anatase TiO₂ nanorod electrode exhibited a discharge capacity of 193 mAh g⁻¹ in the first charge-discharge cycle and showed good cycling performance. However, the obtained reversible capacity was still lower than the theoretical capacity of 335 mAh g⁻¹. In a previous study, we used the Na[FSA]-[C₃C₁pyrr][FSA] (FSA = bis(fluorosulfonyl)amide; C₃C₁pyrr = *N*-methyl-*N*-propylpyrrolidinium) ionic liquid as an electrolyte to investigate the use of carbon-coated nanoscale anatase TiO₂ in SIBs. This TiO₂ negative electrode showed a relatively high reversible capacity of 275 mAh g⁻¹ and good cycling performance at 363 K.²⁶ However, the reversible capacity still needs to be further increased for practical applications.

Fe₂O₃ exhibits high capacity, while anatase TiO₂ shows good cycling performance. If the advantages of these materials are combined, a promising negative electrode material can well be expected. In this work, the electrochemical performance of TiO₂-

^a Graduate School of Energy Science, Kyoto University, Sakyo-ku, Kyoto 606-8501, Japan. E-mail: hagiwara@energy.kyoto-u.ac.jp; tel.: +81-75-753-5822; fax: +81-75-753-5906

^b Institute of Advanced Energy, Kyoto University, Uji 611-0011, Japan. E-mail: nohira.toshiyuki.8r@kyoto-u.ac.jp

Electronic Supplementary Information (ESI) available. See DOI: 10.1039/x0xx00000x

Fe_2O_3 nanocomposites is examined in sodium half-cells using the $\text{Na}[\text{FSA}]\text{-}[\text{C}_3\text{C}_1\text{pyrr}][\text{FSA}]$ ionic liquid as an electrolyte. The $\text{Na}[\text{FSA}]\text{-}[\text{C}_3\text{C}_1\text{pyrr}][\text{FSA}]$ ionic liquid can be used in a wide temperature range and exhibits higher ionic conductivity at higher temperature.²⁷ In order to obtain a high capacity, the temperature of 363 K was adopted. The $\text{TiO}_2\text{-Fe}_2\text{O}_3$ negative electrodes show high reversible capacities above 360 mAh g^{-1} at 10 mA g^{-1} in the first cycle and exhibit good cycling performance at 363 K. Thus, $\text{TiO}_2\text{-Fe}_2\text{O}_3$ negative electrodes are promising electrodes for applying in stationary sodium batteries. However, the $\text{TiO}_2\text{-Fe}_2\text{O}_3$ negative electrodes also present high irreversible capacities in the first cycle, which is one of the main challenges in the future.

Results and discussion

The $\text{TiO}_2\text{-Fe}_2\text{O}_3$ nanocomposites were synthesized by mixing and heating commercially available anatase TiO_2 nanopowders and $\text{Fe}(\text{NO}_3)_3$. Nanocomposites with 10, 20, 30, and 40 wt.% Fe_2O_3 were denoted as $\text{TiO}_2\text{-Fe}_2\text{O}_3\text{-}10$, $\text{TiO}_2\text{-Fe}_2\text{O}_3\text{-}20$, $\text{TiO}_2\text{-Fe}_2\text{O}_3\text{-}30$, and $\text{TiO}_2\text{-Fe}_2\text{O}_3\text{-}40$, respectively. Figure 1 shows the X-ray diffraction (XRD) patterns of the $\text{TiO}_2\text{-Fe}_2\text{O}_3$ nanocomposites with different Fe_2O_3 content, with anatase TiO_2 being the main crystalline phase in all nanocomposites. The diffraction peaks of Fe_2O_3 in $\text{TiO}_2\text{-Fe}_2\text{O}_3\text{-}40$ are very weak, implying that the synthesized Fe_2O_3 in the nanocomposites has poor crystallinity.

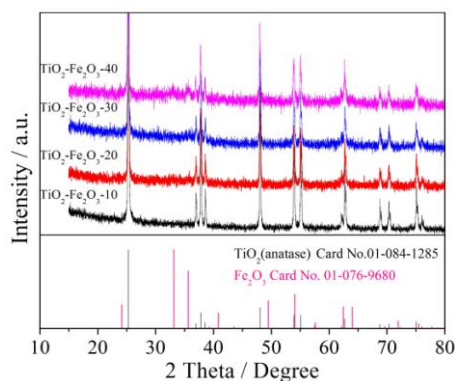


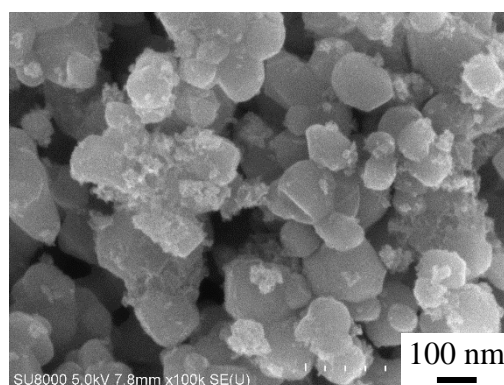
Figure 1. XRD patterns of $\text{TiO}_2\text{-Fe}_2\text{O}_3$ nanocomposites with different Fe_2O_3 content.

Field emission scanning electron microscopy (FE-SEM) image of $\text{TiO}_2\text{-Fe}_2\text{O}_3\text{-}20$ nanocomposites shows the presence of two types of particles (Figure 2a) with sizes of 50–100 and less than 20 nm. The anatase TiO_2 nanopowders have particle sizes of 50–100 nm (Figure S1a), and the synthesized Fe_2O_3 nanopowders in the same condition have a particle size of less than 50 nm (Figure S1b). Thus, it is concluded that the larger particles are TiO_2 and the smaller particles consist of amorphous Fe_2O_3 . Figure 2b presents the energy-dispersive X-ray (EDX) spectrum of $\text{TiO}_2\text{-Fe}_2\text{O}_3\text{-}20$ nanocomposites, showing the presence of Ti, Fe, and O elements with atomic molar fractions of 26.5%, 6.2%, and 67.3%, respectively, which well coincide with the theoretical composition of $\text{TiO}_2\text{-Fe}_2\text{O}_3\text{-}20$. This means that the synthesized powders include TiO_2 and Fe_2O_3 phases, with other nanocomposites ($\text{Fe}_2\text{O}_3\text{-}10$, $\text{TiO}_2\text{-Fe}_2\text{O}_3\text{-}30$, and $\text{TiO}_2\text{-Fe}_2\text{O}_3\text{-}40$) showing similar results.

The electrochemical performance of $\text{TiO}_2\text{-Fe}_2\text{O}_3$ nanocomposites was evaluated at 363 K in half-cells using Na metal as the counter

electrode. Figure 3a shows the charge-discharge curves of the $\text{TiO}_2\text{-Fe}_2\text{O}_3\text{-}20$ electrode at a current rate of $10 \text{ mA (g-TiO}_2\text{-Fe}_2\text{O}_3)^{-1}$ in a voltage range of 0.01–2.5 V. In the first charge-discharge cycle, the $\text{TiO}_2\text{-Fe}_2\text{O}_3\text{-}20$ electrode shows a large charge capacity of $743 \text{ mAh (g-TiO}_2\text{-Fe}_2\text{O}_3)^{-1}$ and exhibits two distinct voltage plateaus between 1.7 and 1.5 V and 0.4 and 0.3 V. The first voltage plateau (1.7 to 1.5 V) is attributable to side-reactions like electrolyte reduction and formation of a solid-electrolyte interphase (SEI),²⁶ while the second one (0.4 to 0.3 V) possibly corresponds to the insertion of Na into $\text{TiO}_2\text{-Fe}_2\text{O}_3$ and further decomposition of the electrolyte.²⁶ The first discharge capacity of the $\text{TiO}_2\text{-Fe}_2\text{O}_3\text{-}20$ electrode is 386 mAh g^{-1} , which is much higher than that of TiO_2 electrodes reported in literature.^{21–24,26} In subsequent cycles, the voltage plateaus disappear, and a stable cycling behavior with a reversible capacity of approximately 360 mAh g^{-1} is observed.

(a)



(b)

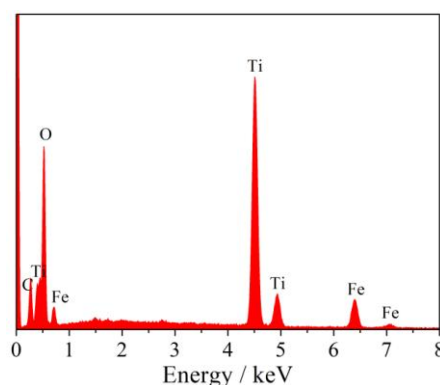


Figure 2. (a) SEM image and (b) EDX spectrum of $\text{TiO}_2\text{-Fe}_2\text{O}_3\text{-}20$ nanocomposites.

Figure 3b shows the first charge-discharge curves of $\text{TiO}_2\text{-Fe}_2\text{O}_3$ electrodes with different Fe_2O_3 content at a current rate of 10 mA g^{-1} . All $\text{TiO}_2\text{-Fe}_2\text{O}_3$ electrodes exhibit similar charge-discharge behavior. With the increase of the Fe_2O_3 content, however, the $\text{TiO}_2\text{-Fe}_2\text{O}_3$ electrodes show higher discharge capacities of 367, 386, 420, and 459 mAh g^{-1} for $\text{TiO}_2\text{-Fe}_2\text{O}_3\text{-}10$, $\text{TiO}_2\text{-Fe}_2\text{O}_3\text{-}20$, $\text{TiO}_2\text{-Fe}_2\text{O}_3\text{-}30$, and $\text{TiO}_2\text{-Fe}_2\text{O}_3\text{-}40$, respectively. The theoretical capacities are 402, 469, 537 and 604 mAh g^{-1} for $\text{TiO}_2\text{-Fe}_2\text{O}_3\text{-}10$, $\text{TiO}_2\text{-Fe}_2\text{O}_3\text{-}20$, $\text{TiO}_2\text{-Fe}_2\text{O}_3\text{-}30$ and $\text{TiO}_2\text{-Fe}_2\text{O}_3\text{-}40$, respectively. Although the obtained discharge capacities are lower than the theoretical capacities, the discharge capacity of $\text{TiO}_2\text{-Fe}_2\text{O}_3$ electrodes increases almost linearly with increasing Fe_2O_3 content, indicating that these nanocomposites are promising high-capacity negative electrode materials for SIBs. Figure 3c shows the first charge-discharge curves

of the TiO_2 and Fe_2O_3 electrodes at a current rate of 10 mA g^{-1} . The discharge capacities are 308 and 672 mAh g^{-1} for the TiO_2 and Fe_2O_3 electrodes, respectively. Since the high capacity results from the high reversible capacity of Fe_2O_3 ,^{14–16} increasing the Fe_2O_3 content can improve the reversible capacity of $\text{TiO}_2\text{-Fe}_2\text{O}_3$ electrodes.

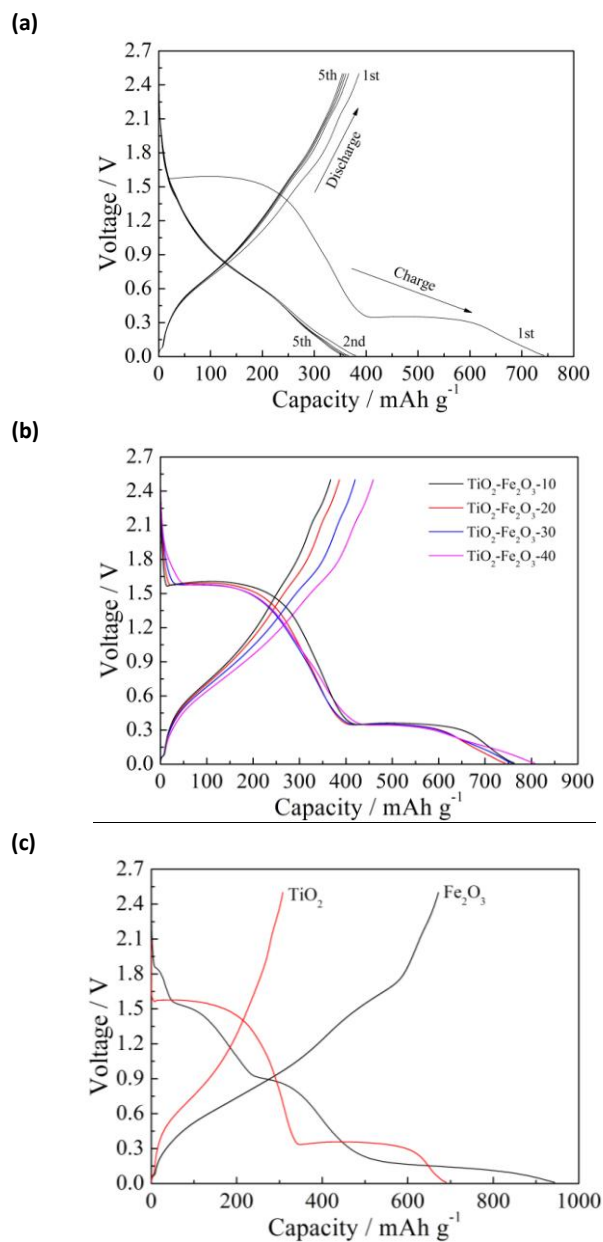


Figure 3. (a) Charge-discharge curves of the $\text{TiO}_2\text{-Fe}_2\text{O}_3\text{-20}$ electrode, (b) the first charge-discharge curves of the $\text{TiO}_2\text{-Fe}_2\text{O}_3$ electrodes with different Fe_2O_3 content, and (c) charge-discharge curves of the TiO_2 and Fe_2O_3 electrodes at a current rate of 10 mA g^{-1} .

According to literature, Fe_2O_3 reversibly reacts with Na ions to form Fe metal and Na_2O during the charge-discharge process.^{14–16} The formation of Fe metal could improve the conductivity and resistance of $\text{TiO}_2\text{-Fe}_2\text{O}_3$ electrodes, which were investigated by electrochemical impedance spectroscopic analysis. Figure S2 shows the Nyquist plots of the $\text{TiO}_2\text{-Fe}_2\text{O}_3\text{-30}$ electrode at different discharge states. As shown in Fig. 3, a small amount of charge-discharge reaction proceeds for the $\text{TiO}_2\text{-Fe}_2\text{O}_3$ electrodes even at the cut-off voltage of 2.5 V. The semicircle at intermediate

frequency is related to the charge-transfer process at the electrode/electrolyte interface. Although the semicircle may consist of charge-transfer process, SEI, and counter electrode reaction,

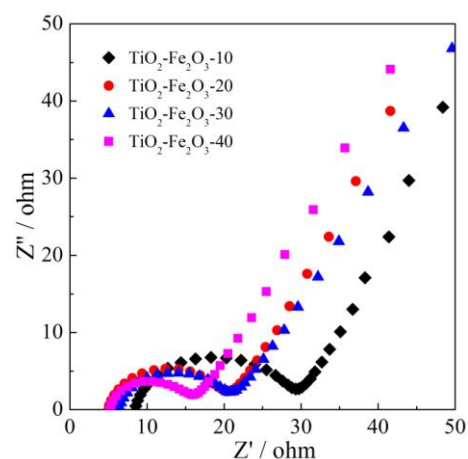


Figure 4. Nyquist plots for $\text{TiO}_2\text{-Fe}_2\text{O}_3$ electrodes with different Fe_2O_3 content after five charge-discharge cycles.

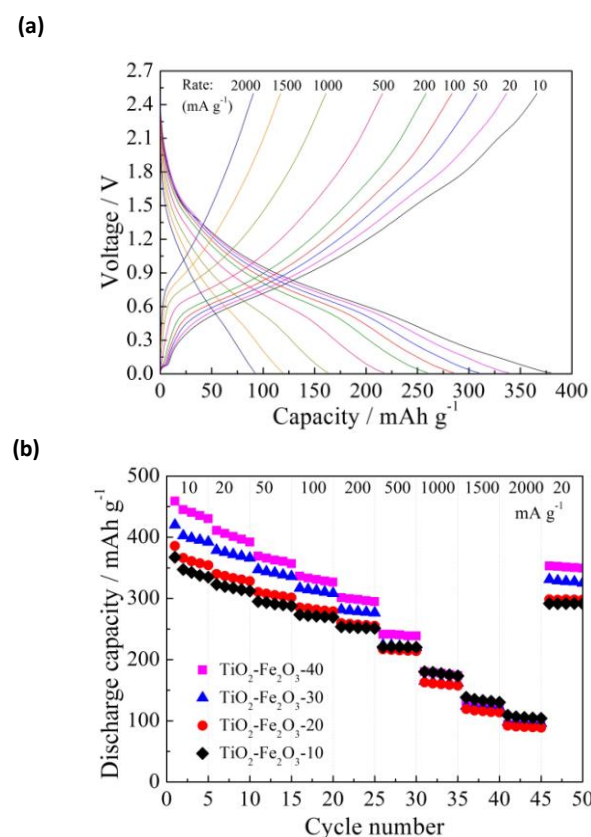


Figure 5. (a) Charge-discharge curves of the $\text{TiO}_2\text{-Fe}_2\text{O}_3\text{-20}$ electrode at current rates of $10\text{--}2000 \text{ mA g}^{-1}$; and (b) rate capabilities of $\text{TiO}_2\text{-Fe}_2\text{O}_3$ electrodes with different Fe_2O_3 content at current rates of $10\text{--}2000 \text{ mA g}^{-1}$.

the charge-transfer process should be the major factor because the impedances from SEI^{28, 29} and counter electrode (Figure S3) are comparatively small. The charge-transfer resistance increases with discharging the electrode from 0.5 V to 2.5 V. Figure 4 shows Nyquist plots of $\text{TiO}_2\text{-Fe}_2\text{O}_3$ electrodes with variable Fe_2O_3 content after five charge-discharge cycles. With increasing Fe_2O_3 content,

the charge-transfer resistance obviously decreases. Thus, the electrochemical performance of $\text{TiO}_2\text{-Fe}_2\text{O}_3$ electrodes is improved by increasing the Fe_2O_3 content.

Rate capability is also an important parameter for describing electrode performance. Figure 5a shows the charge-discharge curves of the $\text{TiO}_2\text{-Fe}_2\text{O}_3\text{-20}$ electrode at current rates of 10–2000 mA g^{-1} . When the current rate is increased, the shapes of the charge-discharge curves remain unchanged. However, the discharge capacities gradually decrease with an increase in current rate. Other $\text{TiO}_2\text{-Fe}_2\text{O}_3$ electrodes also show similar charge-discharge behavior. Figure 5b compares the rate capabilities of $\text{TiO}_2\text{-Fe}_2\text{O}_3$ electrodes with different Fe_2O_3 content. At current rates below 500 mA g^{-1} , $\text{TiO}_2\text{-Fe}_2\text{O}_3$ electrodes with high Fe_2O_3 content show high discharge capacities. However, when the current rate exceeds 500 mA g^{-1} , the effect of Fe_2O_3 content on discharge capacity is attenuated due to the poor capability of Fe_2O_3 at high current rates. $\text{TiO}_2\text{-Fe}_2\text{O}_3\text{-10}$, $\text{TiO}_2\text{-Fe}_2\text{O}_3\text{-20}$, $\text{TiO}_2\text{-Fe}_2\text{O}_3\text{-30}$, and $\text{TiO}_2\text{-Fe}_2\text{O}_3\text{-40}$ show discharge capacities of 107, 91, 97, and 93 mAh g^{-1} at 2000 mA g^{-1} and 253, 258, 280, and 299 mAh g^{-1} at 200 mA g^{-1} , respectively. This suggests that the capacity retention at high current rates is impaired, especially for $\text{TiO}_2\text{-Fe}_2\text{O}_3$ electrodes with high Fe_2O_3 content. In addition, as the current rate is decreased from 2000 to 20 mA g^{-1} , the discharge capacity recovers to high values.

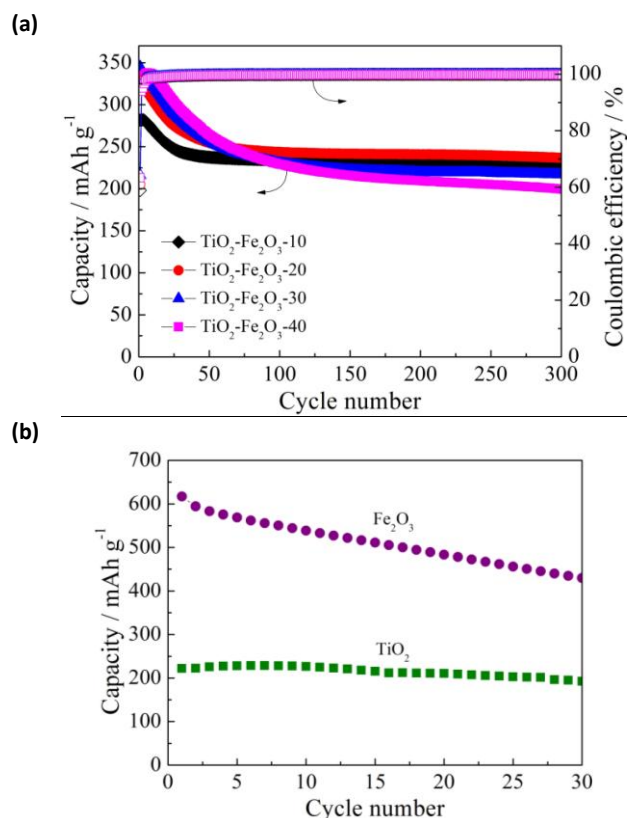


Figure 6. Cycling performance of (a) $\text{TiO}_2\text{-Fe}_2\text{O}_3$ electrodes with different Fe_2O_3 content and (b) TiO_2 and Fe_2O_3 electrodes at a current rate of 200 mA g^{-1} .

Figure 6a shows the cycling performance of $\text{TiO}_2\text{-Fe}_2\text{O}_3$ electrodes with different Fe_2O_3 content at a current rate of 200 mA g^{-1} . For comparison, the cycling performance of the TiO_2 and Fe_2O_3 electrodes at a current rate of 200 mA g^{-1} is shown in Figure 6b. For

all $\text{TiO}_2\text{-Fe}_2\text{O}_3$ electrodes, the discharge capacity decreases quickly in the first 50 cycles, remaining almost unchanged in subsequent cycles. The quick decrease of the discharge capacity is likely attributed to the quick capacity degradation of the Fe_2O_3 , as shown in Figure 6b. $\text{TiO}_2\text{-Fe}_2\text{O}_3$ electrodes with high Fe_2O_3 content show high discharge capacities in the first 50 cycles. However, after 100 cycles, the highest discharge capacity is exhibited by the $\text{TiO}_2\text{-Fe}_2\text{O}_3\text{-20}$ electrode. Except for the initial few cycles, the Coulombic efficiencies for all $\text{TiO}_2\text{-Fe}_2\text{O}_3$ electrodes are higher than 99%. After 300 cycles, the discharge capacities are 227, 237, 217, and 199 mAh g^{-1} for $\text{TiO}_2\text{-Fe}_2\text{O}_3\text{-10}$, $\text{TiO}_2\text{-Fe}_2\text{O}_3\text{-20}$, $\text{TiO}_2\text{-Fe}_2\text{O}_3\text{-30}$, and $\text{TiO}_2\text{-Fe}_2\text{O}_3\text{-40}$, respectively, with the respective capacity retention values being 80%, 72%, 63%, and 60%. This indicates that high Fe_2O_3 content is not beneficial to the cycling performance of $\text{TiO}_2\text{-Fe}_2\text{O}_3$ electrodes, despite increasing the initial capacity.

Conclusions

In summary, the prepared $\text{TiO}_2\text{-Fe}_2\text{O}_3$ nanocomposites were evaluated as negative electrode materials for rechargeable sodium-ion batteries using the $\text{Na}[\text{FSA}]\text{-}[\text{C}_3\text{C}_1\text{pyrr}][\text{FSA}]$ ionic liquid as an electrolyte. These nanocomposites consisted of anatase TiO_2 and amorphous Fe_2O_3 particles with sizes of 50–100 nm and less than 20 nm, respectively. The $\text{TiO}_2\text{-Fe}_2\text{O}_3$ electrodes exhibit high reversible capacities, with discharge capacities of 367, 386, 420, and 459 mAh g^{-1} at 10 mA g^{-1} for $\text{TiO}_2\text{-Fe}_2\text{O}_3$ electrodes with 10, 20, 30 and 40 wt.% Fe_2O_3 , respectively. In addition, these electrodes also show good rate capability and cycling performance, with Fe_2O_3 content affecting both of these parameters. These results suggest that $\text{TiO}_2\text{-Fe}_2\text{O}_3$ nanocomposites are attractive high-capacity negative electrode materials for ionic liquid-based sodium-ion secondary batteries.

Experimental

Commercially available anatase TiO_2 nanopowders (Sigma Aldrich) and $\text{Fe}(\text{NO}_3)_3\cdot 9\text{H}_2\text{O}$ (Wako) were used as raw materials to synthesize $\text{TiO}_2\text{-Fe}_2\text{O}_3$ nanocomposites. $\text{Fe}(\text{NO}_3)_3\cdot 9\text{H}_2\text{O}$ was dissolved in ethanol, with the anatase TiO_2 nanopowders subsequently dispersed in this solution by stirring. The mixture was dried at 333 K and heated at 573 K for 3 h to obtain $\text{TiO}_2\text{-Fe}_2\text{O}_3$ nanocomposites, which were synthesized with 10, 20, 30 and 40 wt.% Fe_2O_3 . For comparison, Fe_2O_3 nanopowders were also synthesized under the same conditions. The crystal structure and morphology of these nanocomposites were investigated by X-ray diffraction (XRD, Rigaku SmartLab) and field emission scanning electron microscopy (FE-SEM, Hitachi SU8000) with energy-dispersive X-ray spectroscopy (EDX).

Electrochemical characterization was performed using coin-type 2032 cells with sodium foil as counter-electrodes. $\text{TiO}_2\text{-Fe}_2\text{O}_3$ working electrodes were fabricated using a conventional coating method. A slurry consisting of $\text{TiO}_2\text{-Fe}_2\text{O}_3$ nanocomposites (80 wt.%), acetylene black (10 wt.%), and polyamide-imide (10 wt.%) in *N*-methyl-2-pyrrolidone (NMP) was prepared and uniformly spread onto Al foil. The

polyamide-imide was used in this study because it has higher chemical stability and mechanical strength at high temperatures compared to conventional polyvinylidene fluoride (PVDF). The obtained TiO₂-Fe₂O₃ electrodes were dried in vacuum at 393 K overnight before being transferred into an Ar-filled glove box. For comparison, the TiO₂ and Fe₂O₃ electrodes were also fabricated under the same conditions. The Na[FSA]-[C₃C₁pyrr][FSA] ionic liquid with a molar ratio of 2:8 was used as an electrolyte. A glass fiber filter (Whatman, GF-A, 260 mm) was used as a separator. The TiO₂-Fe₂O₃ electrodes and separators were vacuum-impregnated with Na[FSA]-[C₃C₁pyrr][FSA] before being assembled into coin cells. Charge-discharge tests were conducted at constant current rates of 10–2000 mA g⁻¹ in a voltage range of 0.01–2.5 V at 363 K. Electrochemical impedance measurements for TiO₂-Fe₂O₃ electrodes after charge-discharge cycles were performed in the frequency range of 200 kHz to 100 mHz using an AC voltage signal of 10 mV.

Acknowledgements

This study was partly supported by the Advanced Low Carbon Technology Research and Development Program (ALCA, No. 3428) of the Japan Science and Technology Agency (JST) and the Elements Strategy Initiative to Form Core Research Center program of the Japanese Ministry of Education, Culture, Sports, Science and Technology (MEXT).

Notes and references

1. L. Wu, X. H. Hu, J. F. Qian, F. Pei, F. Y. Wu, R. J. Mao, X. P. Ai, H. X. Yang and Y. L. Cao, *Energy Environ. Sci.*, 2014, **7**, 323.
2. J. W. Wang, X. H. Liu, S. X. Mao and J. Y. Huang, *Nano Lett.*, 2012, **12**, 5897.
3. L. F. Xiao, Y. L. Cao, J. Xiao, W. Wang, L. Kovarik, Z. M. Nie and J. Liu, *Chem. Commun.*, 2012, **48**, 3321.
4. Y. H. Xu, Y. J. Zhu, Y. H. Liu and C. S. Wang, *Adv. Energy Mater.*, 2013, **3**, 128.
5. R. Alcántara, J. M. Jimenez-Mateos, P. Lavela and J. L. Tirado, *Electrochem. Commun.*, 2001, **3**, 639.
6. K. Tang, L. J. Fu, R. J. White, L. H. Yu, M. M. Titirici, M. Antonietti and J. Maier, *Adv. Energy Mater.*, 2012, **2**, 873.
7. J. Ding, H. L. Wang, Z. Li, A. Kohandehghan, K. Cui, Z. W. Xu, B. Zahiri, X. H. Tan, E. M. Lotfabad, B. C. Olsen and D. Mitlin, *ACS Nano*, 2013, **7**, 11004.
8. S. Komaba, W. Murata, T. Ishikawa, N. Yabuuchi, T. Ozeki, T. Nakayama, A. Ogata, K. Gotoh and K. Fujiwara, *Adv. Funct. Mater.*, 2011, **21**, 3859.
9. J. Zhao, L. W. Zhao, K. Chihara, S. Okada, J. Yamaki, S. Matsumoto, S. Kuze and K. Nakane, *J. Power Sources*, 2013, **244**, 752.
10. W. Wang, C. J. Yu, Y. J. Liu, J. G. Hou, H. M. Zhu and S. Q. Jiao, *RSC Adv.*, 2013, **3**, 1041.
11. A. Rudola, K. Saravanan, C. W. Mason and P. Balaya, *J. Mater. Chem. A*, 2013, **1**, 2653.
12. J. Xu, C. Z. Ma, M. Balasubramanian and Y. S. Meng, *Chem. Commun.*, 2014, **50**, 12564.
13. D. Wu, X. Li, B. Xu, N. Twu, L. Liu and G. Ceder, *Energy Environ. Sci.*, 2015, **8**, 195.
14. M. Valvo, F. Lindgren, U. Lafont, F. Bjorefors and K. Edstrom, *J. Power Sources*, 2014, **245**, 967.
15. Z. L. Jian, B. Zhao, P. Liu, F. J. Li, M. B. Zheng, M. W. Chen, Y. Shi and H. S. Zhou, *Chem. Commun.*, 2014, **50**, 1215.
16. Y. Z. Jiang, M. J. Hu, D. Zhang, T. Z. Yuan, W. P. Sun, B. Xu and M. Yan, *Nano Energy*, 2014, **5**, 60.
17. S. B. Wang, W. Wang, P. Zhan and S. Q. Jiao, *Chemelectrochem*, 2014, **1**, 1636.
18. H. Xiong, M. D. Slater, M. Balasubramanian, C. S. Johnson and T. Rajh, *J. Phys. Chem. Lett.*, 2011, **2**, 2560.
19. J. P. Huang, D. D. Yuan, H. Z. Zhang, Y. L. Cao, G. R. Li, H. X. Yang and X. P. Gao, *RSC Adv.*, 2013, **3**, 12593.
20. J. C. Perez-Flores, C. Baetz, A. Kuhn and F. Garcia-Alvarado, *J. Mater. Chem. A*, 2014, **2**, 1825.
21. Y. Xu, E. M. Lotfabad, H. Wang, B. Farbod, Z. Xu, A. Kohandehghan and D. Mitlin, *Chem. Commun.*, 2013, **49**, 8973.
22. K. T. Kim, G. Ali, K. Y. Chung, C. S. Yoon, H. Yashiro, Y. K. Sun, J. Lu, K. Amine and S. T. Myung, *Nano Lett.*, 2014, **14**, 416.
23. L. Wu, D. Buchholz, D. Bresser, L. Gomes Chagas and S. Passerini, *J. Power Sources*, 2014, **251**, 379.
24. X. M. Yang, C. Wang, Y. C. Yang, Y. Zhang, X. N. Jia, J. Chen and X. B. Ji, *J. Mater. Chem. A*, 2015, **3**, 8800.
25. H. Usui, S. Yoshioka, K. Wasada, M. Shimizu and H. Sakaguchi, *ACS Appl. Mater. Interfaces*, 2015, **7**, 6567.
26. C. S. Ding, T. Nohira and R. Hagiwara, *J. Mater. Chem. A*, 2015, **3**, 20767.
27. C. S. Ding, T. Nohira, R. Hagiwara, K. Matsumoto, Y. Okamoto, A. Fukunaga, S. Sakai, K. Nitta and S. Inazawa, *J. Power Sources*, 2014, **269**, 124.
28. T. Hang, D. Mukoyama, H. Nara, T. Yokoshima, T. Momma, M. Li and T. Osaka, *J. Power Sources*, 2014, **256**, 226.
29. C. F. Chen and P. P. Mukherjee, *Phys. Chem. Chem. Phys.*, 2015, **17**, 9812.